Journal of Alloys and Compounds 968 (2023) 171986

Contents lists available at ScienceDirect

Journal of Alloys and Compounds

journal homepage: www.elsevier.com/locate/jalcom

Chemistry-structure-property relations in $Al_{10}Cr_{15}(Fe_3Mn)_{75-x}(Ni)_x$ medium-entropy alloys

Jarrod Gesualdi, Peyman Asghari-Rad, Erik Furton, Abhishek Singh, Allison Beese, Hojong Kim *

Materials Science and Engineering, The Pennsylvania State University, 406 Steidle Building, University Park, PA 16802, United States

ARTICLE INFO

Keywords:
Alloy design
High-entropy alloy
Corrosion properties
Precipitation hardening

ABSTRACT

The microstructure, phase behavior, mechanical properties, and corrosion properties of a series of $Al_{10}Cr_{15}(Fe_3Mn)_{75-x}(Ni)_x$ medium-entropy alloys (MEAs) spanning 0–20 at% Ni were studied to elucidate the chemistry-structure-property relationship of this system as a function of Ni content. This work demonstrates that from an initial BCC phase $Al_{10}Cr_{15}(Fe_3Mn)_{75}$ MEA, Ni additions of 5 and 10 at% result in the formation of ordered B2-phase precipitates due to interaction of Ni with Al, resulting in high hardness (~475 HV). Further Ni addition to 15 at% leads to a dual-phase FCC+BCC structure, with B2 phase precipitates distributed in the BCC matrix relatively rich in Al and Ni but depleted in Cr. This dual-phase structure has a high yield strength (YS) of 600 MPa with a total elongation of 15%. Additionally, the B2 precipitates in BCC phase serve as preferential sites for corrosion in 0.6 M NaCl. Increasing Ni content to 20 at% results in lower YS of 300 MPa, but a significant improvement in ductility and corrosion resistance due to the increased FCC phase fraction.

1. Introduction

Both mechanical properties and corrosion resistance of materials are vital for numerous engineering applications. Corrosion resistance is necessary to protect materials from degradation caused by chemical reactions with the environment. Meanwhile, good mechanical strength and ductility are required to withstand mechanical forces and stresses without fracturing. Ongoing efforts in the field of materials science are dedicated to the development of new alloys with exceptional mechanical properties and corrosion resistance. These endeavors stem from the necessity to meet the rigorous demands of diverse industries and applications. The concept of multi-principal element alloys (MPEAs) has introduced a promising avenue for alloy design, where MPEAs are classified as either high-entropy alloys (HEAs) or medium entropy alloys (MEAs) based on their configurational entropy [1–4]. This innovative approach provides opportunities to develop new materials with outstanding mechanical properties and corrosion resistance. HEAs, comprising multiple principal elements in equal or near-equal atomic proportions, exhibit complex microstructures, which contribute to their exceptional mechanical and corrosion-resistant properties.

The AlCrFeMnNi alloy system is a class of MPEAs that has been shown to have good corrosion resistance and high strength. Incorporating lightweight Al in the alloy reduces overall density, while Mn serves as a cost-effective element that stabilizes the face-centered cubic (FCC) structure, acting as a substitute for the expensive Co element. The studies conducted so far have investigated the unique properties of AlCrFeMnNi equiatomic composition with both body-centered cubic (BCC) and B2 phases [5–8]. However, there are a limited number of systematic investigations focusing on non-equiatomic compositions. These studies are crucial as they provide opportunities to explore how modifications in alloy chemistry can fine-tune properties such as phase behavior, mechanical strength, and corrosion resistance.

Chen et al. probed the effect of Al content on $Al_xCrFeMn_{0.8}Ni_{2.1}$ alloys and demonstrated that from the initial CrFeMnNi alloy, Al addition resulted in the transition from FCC to BCC and formation of ordered BCC phase [9]. As Al content increased, hardness increased due to B2 and BCC phase formation. However, corrosion resistance in 1 M NaCl solution declined significantly due to selective corrosion of the AlNi-rich, Cr-poor phase. The as-cast nature of the samples makes it unclear whether thermal treatment such as homogenization might improve the alloy properties, as micrographs indicated a dendritic/interdendritic microstructure with strong chemical segregation between these regions. The work by Shi et al. studying $Al_xCoCrFeNi$ alloys as a function of both Al content, as well as exploring the effect of homogenization, showed

* Corresponding author.
E-mail address: huk29@psu.edu (H. Kim).

https://doi.org/10.1016/j.jallcom.2023.171986
Received 21 June 2023; Received in revised form 18 August 2023; Accepted 30 August 2023
Available online 1 September 2023

similarly that as Al content increased, BCC/B2 phase fraction increased, and corrosion resistance in 0.6 M NaCl decreased [10]. However, they demonstrated that heat treatment of the alloy could improve corrosion resistance by homogenizing the microstructure and reducing chemical inhomogeneity. The effect of homogenization in this study transitioned the material from fine-grained to coarse-grained equiaxed microstructures, highlighting the importance of the casting technique on the material properties in as-cast studies when comparing across literature sources.

Unlike previous studies that primarily concentrated on the addition of Al to CrFeMnNi alloy system [9,11–14], the present research systematically modifies a BCC-based $Al_{10}Cr_{15}(Fe_3Mn)_{75}$ MEA by introducing Ni in various contents. The addition of Ni serves the purpose of stabilizing the FCC phase and facilitating the formation of AlNi-rich precipitates. This deliberate modification aims to achieve a synergistic enhancement in both mechanical performance and corrosion resistance. This research encompasses a thorough analysis of the microstructure of the homogenized samples, enabling the determination of local chemistry, local phase behavior, and a detailed characterization of the ordered phase present in these MEAs. This microstructural information is utilized to understand the chemistry-structure-property relationship of $Al_{10}Cr_{15}(Fe_3Mn)_{75-x}(Ni)_x$ MEAs as a function of Ni content. The study encompasses measurements of hardness, uniaxial tensile tests, and electrochemical polarization measurements in 0.6 M NaCl to assess the mechanical properties and corrosion resistance.

2. Experimental methods

2.1. Alloy fabrication

$Al_{10}Cr_{15}(Fe_3Mn)_{75-x}(Ni)_x$ MEAs, presented in Table 1, were prepared by first weighing appropriate amounts of Al (>99%, Alfa Aesar), Cr (99.995%, Alfa Aesar), Fe (>99.9%, Allied Metals Corporation), Mn (>99.9%, Allied Metals Corporation), and Ni (99.9%, Alfa Aesar). The MEAs were fabricated using an arc melting furnace (MAM-1, Edmund-Buhler) under an inert argon atmosphere by remelting at least four times to reach a uniform composition, and formed into 1 cm diameter button-shaped samples. Homogenization of alloys was performed at 1100 °C for 2 h in air (Carbolite BLF 1700 furnace). Quenching was conducted by promptly removing the alloy from the furnace at temperature and immersing it into a vessel of room temperature water.

The alloy chemistry in this study was determined based on the following rationale: Fe was modified with Mn at a 3:1 ratio to encourage FCC formation by Mn but to still retain an Fe majority. Cr was fixed at 15 at% to achieve a base level of corrosion resistance, as a minimum of 13 at% is necessary for pitting resistance in chloride environments [15]. Al content was fixed at 10 at% to reduce the alloy density, while remaining low enough that it was feasible to stabilize the FCC phase with sufficient Ni addition. Ni was added at the expense of Fe and Mn to maintain the lower density afforded by Al, corrosion resistance afforded by Cr, and maintain a majority of Fe content in the alloy.

2.2. Characterization

X-ray Diffraction (XRD) analysis (Panalytical, Empyrean II) was conducted from $20° \leq 2\theta \leq 105°$ using Co-Kα radiation and analyzed by JADE software (MDI Jade 2010) from samples mounted in phenolic resin by hot mounting press, and polished to 1200 grit using SiC papers. For microstructural characterization, the homogenized alloy samples were mounted in phenolic resin and ground with SiC papers, polished with diamond suspensions to 1 μm and colloidal silica suspension to 0.02 μm. Backscattered electron (BSE) imaging and energy dispersive X-ray spectroscopy (EDS) were performed in a field-emission scanning electron microscope (FESEM, Apreo S). Electron backscattered diffraction (EBSD) was performed with samples held at a 70° tilt in a FESEM equipped with an EBSD detector (Oxford Symmetry). Samples for transmission electron microscope (TEM) analysis were prepared from homogenized alloy specimens by focused ion beam (FIB) (FEI Helios Nanolab 660). Samples prepared by FIB were analyzed with TEM (FEI Titan^3 G2) equipped with an EDS detector (Super-X). Sample imaging and EDS measurements were performed under scanning transmission electron microscope (STEM) mode.

2.3. Mechanical testing

For Vickers microhardness testing, the homogenized alloys (1 cm diameter buttons) were mounted into phenolic resin by hot mounting press (Allied TechPress 3, Allied High Tech) and polished to 1200 grit. Hardness was measured using a Vickers microhardness tester (HM200, Mitutoyo) and determined from the average of ten indents, each spaced approximately four times the diagonal length of the Vickers indent, in accordance with ASTM E384 [16]. A maximum indent force of 1 kgf was used, with 5 s load time, 10 s dwell time, and 5 s unload time. Error reported is the standard deviation from the mean value of hardness measured.

For uniaxial tensile testing, homogenized samples were machined using wire EDM (electrical discharge machining) to form dog-bone-shaped specimens (gauge length: 2.19 mm, width: 1.5 mm, thickness: 1 mm), and mechanically tested with a custom-built miniature load frame with a 4500 N load cell. The crosshead displacement rate was 1 μm/s, corresponding to a quasi-static strain rate of approximately $7 \times 10^{-4}\ s^{-1}$. Three samples were tested for each composition. Displacement was measured with digital image correlation (DIC), a non-contact technique which measures surface deformation. The sample was coated with a white basecoat, followed by application of a black speckled pattern. A digital camera (GRAS-50S5M-C, Teledyne FLIR) with a resolution of approximately 5 μm/px recorded images during mechanical testing at a rate of 1 Hz, and the deformation history was reconstructed with digital image correlation software (VIC-2D, Correlated Solutions). Virtual extensometers had initial length of 1.5 mm.

2.4. Corrosion testing

Electrochemical measurements of alloys were performed in a three-electrode electrochemical cell using a potentiostat/galvanostat (Autolab PGSTAT-302 F). The potential was measured using an Ag/AgCl reference electrode (RE) (4 M KCl) introduced by a Luggin-Haber capillary and platinum mesh served as the counter electrode (CE). Working electrodes (WEs) were arc-melted and homogenized specimens (1 cm in diameter), connected to Cu wire, and cast into epoxy resin. The

Table 1
Nominal chemical compositions, configurational entropy ($\Delta S_{conf.}$), and theoretical density of the MEAs developed in the present study.

Alloy	Nominal chemical composition (at%)					$\Delta S_{conf.}$	Density (g/cm^3)
	Al	Cr	Fe	Mn	Ni		
$Al_{10}Cr_{15}(Fe_3Mn)_{75}$	10.00	15.00	56.25	18.75	-	-1.15 R	6.96
$Al_{10}Cr_{15}(Fe_3Mn)_{70}Ni_5$	10.00	15.00	52.50	17.50	5.00	-1.31 R	7.01
$Al_{10}Cr_{15}(Fe_3Mn)_{65}Ni_{10}$	10.00	15.00	48.75	16.25	10.00	-1.39 R	7.06
$Al_{10}Cr_{15}(Fe_3Mn)_{60}Ni_{15}$	10.00	15.00	45.00	15.00	15.00	-1.44 R	7.11
$Al_{10}Cr_{15}(Fe_3Mn)_{55}Ni_{20}$	10.00	15.00	41.25	13.75	20.00	-1.47 R	7.16

mounted samples were ground and polished to 1200 grit and sonicated in isopropanol for 5 min immediately prior to cell assembly to reveal a fresh metal surface. The electrodes were then masked with electroplater's tape to isolate a fixed surface area (0.178 cm^2).

Electrolyte was prepared from NaCl (≥99%, Sigma-Aldrich) in distilled water. The electrolyte in the cell was sparged with nitrogen gas for 1 h for de-aeration and the atmosphere was under continuous nitrogen gas flow throughout the experiment. Potentiodynamic polarization measurements were performed with a sweep rate of 600 mV h^{-1} following ASTM standard (G5–14) [17]. After polarization testing, each sample was removed from the solution, rinsed thoroughly with distilled water, and sonicated for 10 mins in isopropanol to remove loose corrosion products, followed by characterization by optical microscope (Axiovert 200. Zeiss) equipped with a CCD camera.

3. Results and discussion

3.1. Microstructure evolution as a function of Ni content

Microstructural evolution as a function of systematic Ni addition to the $Al_{10}Cr_{15}(Fe_3Mn)_{75-x}(Ni)_x$ alloy system was analyzed using XRD, as shown in Fig. 1. At 0 at% Ni, the characteristic (200) and (211) reflections for the BCC phase were detected. The constraint on reflections to these peaks is probably a consequence of the pronounced texturing phenomenon present in this sample. After adding 5 and 10 at% Ni, along with the BCC phase, a (100) reflection consistent with an ordered phase appears. Addition of 15 at% Ni resulted in FCC phase formation while retaining the BCC and ordered phases. A further addition to 20 at% Ni shows the relative peak heights for FCC and BCC shift, increasing for FCC and decreasing for BCC/ordered phases compared to 15 at% Ni. Furthermore, the asymmetry in the peaks corresponding to the (200) and (211) reflections is noticeable in the samples that contain the ordered phase. This phenomenon might arise from the overlap of peaks between the BCC and ordered phase, owing to their close lattice parameters. From these data, it can be concluded that Ni addition has two core effects: stabilization of an ordered phase and stabilization of the FCC phase in the structure. Further analysis is performed to identify the ordered phase, which is discussed in the following.

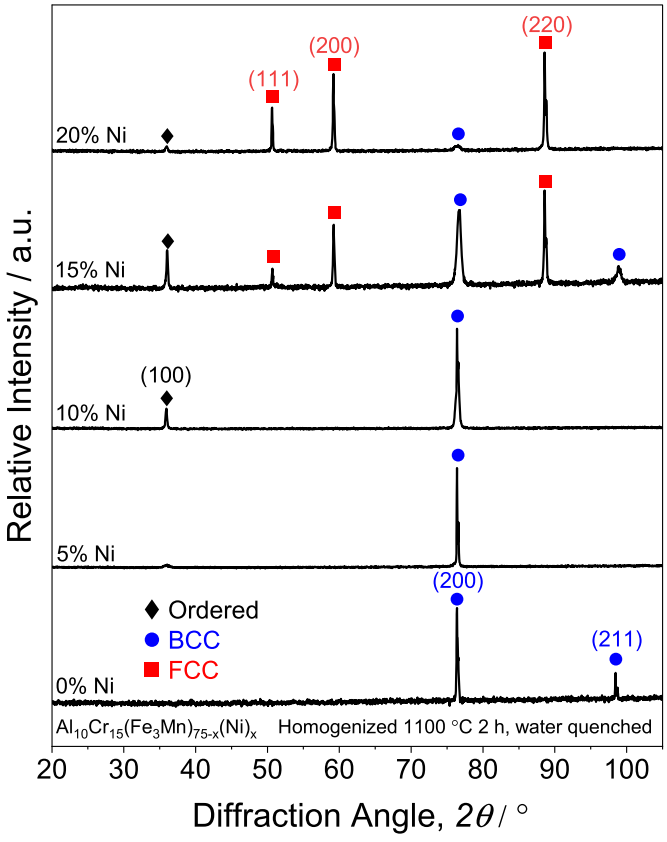

Fig. 1. X-ray diffraction measurements of homogenized $Al_{10}Cr_{15}(Fe_3Mn)_{75-x}(Ni)_x$ MEAs as a function of Ni content.

To better understand the microstructural evolution as Ni is added to the $Al_{10}Cr_{15}(Fe_3Mn)_{75-x}(Ni)_x$ alloy system, Fig. 2 shows BSE images at low magnifications (a1–e1) and respective high magnifications (a2–e2) for each composition. Fig. 2(a) and (b) (0 and 5 at% Ni) demonstrate a microstructure characteristic of a single-phase material with equiaxed grains. Fig. 2(c) reveals the presence of numerous uniformly distributed precipitates in the microstructure of the 10 at% Ni MEA. This suggests that the ordered phase detected by XRD in Fig. 1 appears as nano-scaled (<50 nm) precipitates in the 10 at% Ni MEA. Further Ni addition to 15 at% (Fig. 2d) shows a significant change in the microstructure, likely due to the emergence of the FCC phase. The following structure is observed at low magnification (Fig. 2(d1)): large grains spanning tens of microns (similar to Fig. 2a) and smaller grains emerging both from grain boundaries and within grains with a platelet-type microstructure. At higher magnification (Fig. 2(d2)), a secondary structure is apparent at this length scale: the platelet-shaped grains appear entirely free of precipitates, and the medium between them, which appeared to be homogeneous at low magnifications, consists of one continuous phase within which are cuboidal precipitates on the order of 100–200 nm, and finer cuboidal precipitates < 100 nm in size. As Ni content is increased to 20 at% (Fig. 2(e1)), these platelet grains appear to grow in fraction, resulting in a relatively fine-grained microstructure free of precipitates but including regions between platelet grains that are visually distinct and appear precipitate-free (Fig. 2(e2)).

At these elevated Ni contents (15 and 20 at%), due to the complexity of the microstructure evident by the XRD analysis (Fig. 1) and BSE imaging (Fig. 2), it became essential to elucidate local phase behavior and chemistry in these MEAs by EBSD and EDS analyses (Fig. 3). Shown in Fig. 3a, the EBSD-phase mapping of the MEA with 15 at% Ni demonstrates that the phase at grain boundaries and as platelets within grains are the FCC structure, while the continuous phase within grains is the BCC structure. The EDS results in Figs. 3b and 3c reveal the overall composition of the regions corresponding to the FCC and BCC regions. The FCC region with a phase fraction (F_{FCC}) of 54% is richer in Ni and Fe, while the BCC region with a fraction (F_{BCC}) of 46% is richer in Al and Cr. The EBSD does not detect the precipitates observed in Fig. 2(d2) since the EBSD analysis is performed on a large scale to evaluate the general phase distribution in the MEA with 15 at% Ni.

By an increase in the Ni content to 20 at%, EBSD-phase mapping presented in Fig. 3d displays that the FCC phase fraction grows significantly to 91%, which is in agreement with the phase evolutions illustrated in Fig. 1. The EDS measurements shown in Fig. 3e and 3f demonstrate that Al and Ni are concentrated in the BCC phase, and Fe and Cr are concentrated in the FCC phase. In the Al and Ni-containing MEAs/HEAs, the formation of AlNi-rich precipitates with a B2 (ordered BCC) structure has been reported [5,14]. The enrichment of Al and Ni elements in the BCC phase observed in Fig. 3 f, along with the (001) reflections of an ordered phase detected by the XRD (Fig. 1), could confirm that the AlNi-rich precipitates in the 20 at% Ni MEA are attributed to the B2 structure. Also, some regions are detected with a higher concentration of Cr (marked by an arrow in Fig. 3e), which could be related to sigma phase formation, previously observed by other authors, in AlCrFeMnNi alloys after aging below 900 °C [13,18]. However, the XRD analysis does not detect the sigma phase (Fig. 1), likely due to a low fraction in the 20 at% Ni MEA.

As the prior analysis by EBSD and EDS left the location of the ordered phase anticipated in the microstructure undetermined, further investigation into the microstructure was necessary for the $Al_{10}Cr_{15}(Fe_3Mn)_{60}Ni_{15}$ alloy. The BSE micrographs revealed nano-scale precipitates contained within the continuous BCC phase (Fig. 2d),

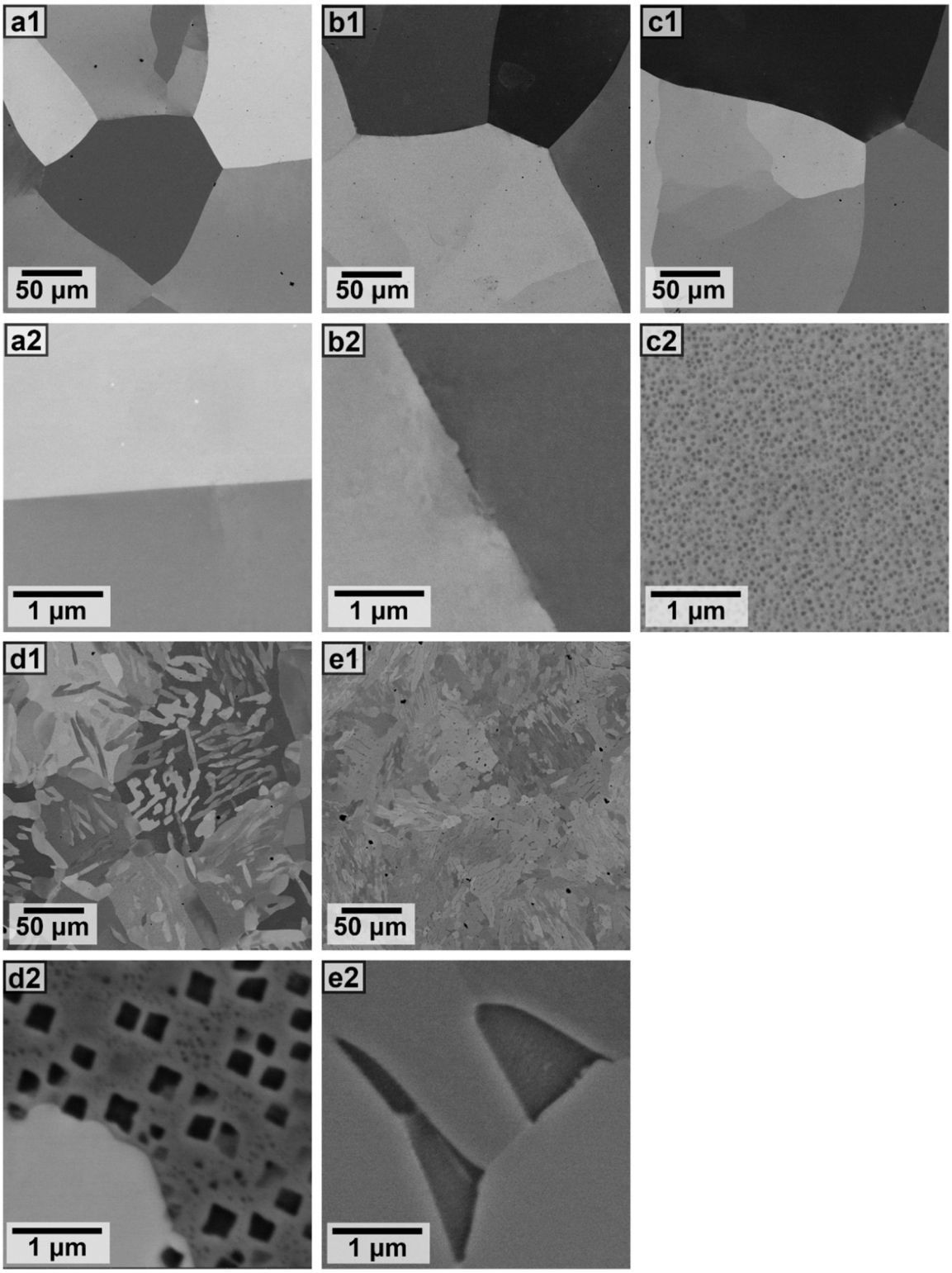

Fig. 2. Backscattered electron images of $Al_{10}Cr_{15}(Fe_3Mn)_{75-x}(Ni)_x$ MEAs as a function of Ni content; (a1) 0% Ni, (b1) 5% Ni, (c1) 10% Ni, (d1) 15% Ni, (e1) 20% Ni, (a2-e2) higher magnifications respective to (a1-e1).

which were undetectable by the relatively large-scale EBSD (Fig. 3a). For this reason, STEM analysis was performed and is demonstrated in Fig. 4a, where a section of the BCC phase region containing those precipitates is shown. The selected area electron diffraction (SAED) patterns of three distinct regions in the microstructure (Fig. 4b) demonstrate the following: Region 1, the continuous matrix phase consists of the BCC structure; Region 2, the cuboidal precipitates on the order of 100–200 nm consist of the ordered B2 structure, evidenced by the pronounced superlattice diffraction spots; Region 3, the finer precipitates < 100 nm in width, consist of the ordered B2 structure. It is important to note that the fine precipitates are distributed throughout the BCC matrix, resulting in excessive superlattice spots in the SAED pattern on the

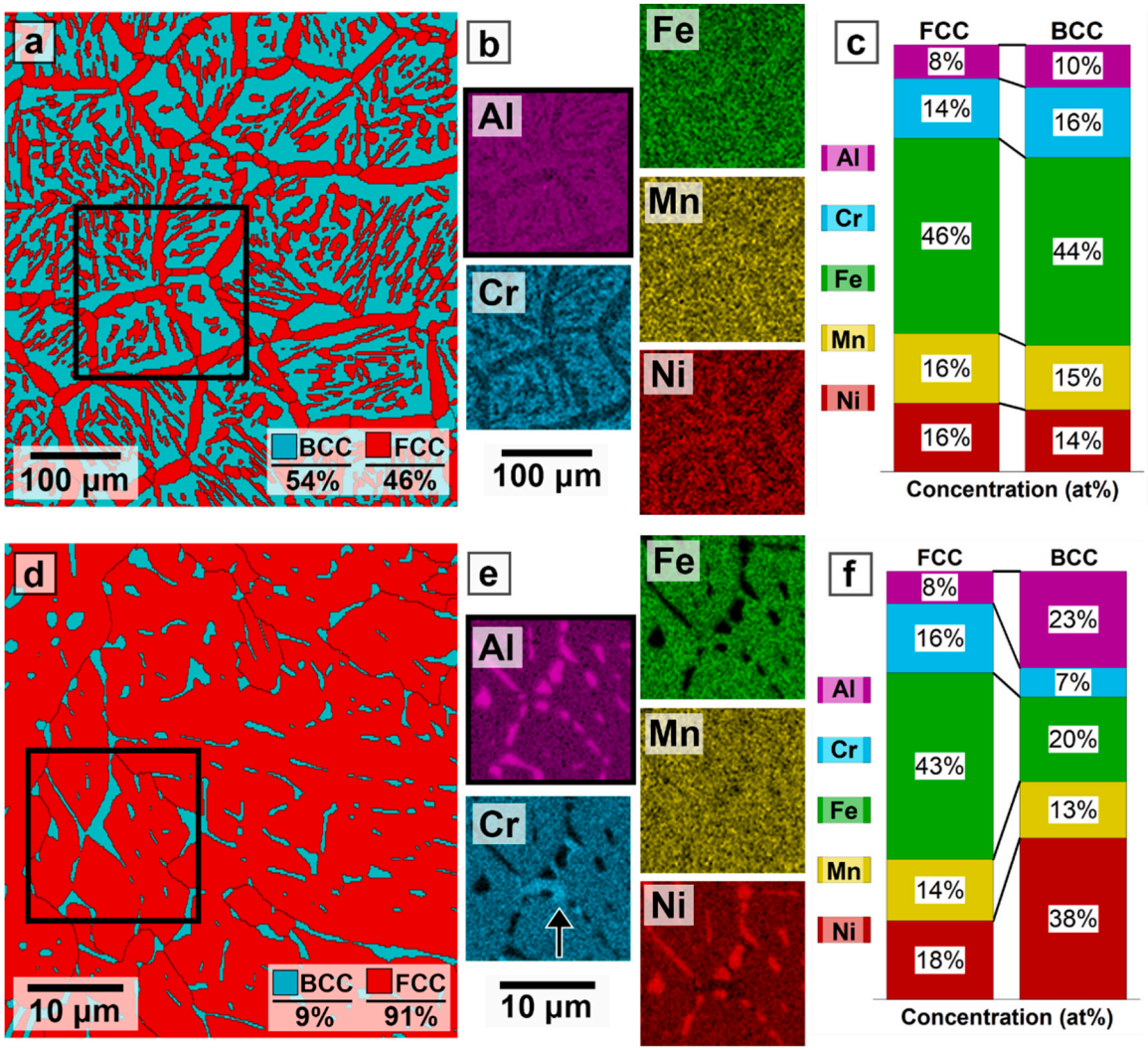

Fig. 3. (a, d) EBSD-phase maps, (b, e) EDS maps, and (c, f) EDS quantification by point scans for the $Al_{10}Cr_{15}(Fe_3Mn)_{75-x}(Ni)_x$ MEAs with (a-c) 15 at% Ni and (d-f) 20 at% Ni.

BCC phase matrix in Fig. 4b.

The corresponding TEM-EDS maps and quantitative EDS analysis of different regions are presented in Fig. 4c and d. The matrix BCC phase (Region 1) is predominantly enriched in Fe (53 at%) and Cr (19 at%) with low solubility of Al (4 at%) while the cuboidal precipitates (Region 2) consist of 50 at% Ni and 18 at% Al with a minor concentration of 2 at % for Cr. The present cuboidal morphology of the AlNi-rich B2 precipitates is a distinctive morphology among the previously reported AlNi-containing MEAs/HEAs [19,20]. The fine precipitates (Region 3) also represent an AlNi-rich composition but with a considerably high Fe content compared to the coarser cuboidal precipitates. Due to their small size, however, it is likely this EDS signal is a mixture of the matrix and precipitates, but it still suggests relative enrichment of Al and Ni, and depletion of Cr. Interestingly, Mn is uniformly distributed throughout the microstructure with a concentration of about 15 at%, similar to its nominal content in this MEA.

HR-STEM imaging was performed to clarify the structure of the fine precipitates corresponding to Region 3, shown in Fig. 4e and f. According to Fig. 4e, the fine precipitates also have a cuboidal morphology. Fig. 4f displays the boundary of the fine precipitate with the matrix, and corresponding fast Fourier transform (FFT) SAED patterns of the marked regions are presented in Fig. 4g. The FFT-SAED pattern of the matrix demonstrates the BCC structure spots, and the pattern of the fine precipitate represents an ordered B2 structure, confirming the results illustrated in Fig. 4b.

Drawing from the microstructural analyses presented in Figs. 1 to 4, the evolution of microstructure upon the introduction of Ni into the base $Al_{10}Cr_{15}(Fe_3Mn)_{75}$ MEA can be concisely summarized. Both the base MEA and the 5 at% Ni MEA exhibit a single-phase BCC structure, indicating that the 5 at% Ni addition effectively integrated into the matrix as a solid solution without the emergence of a secondary phase. Meanwhile, the incorporation of 10 at% Ni triggers the appearance of fine B2 precipitates within the MEA structure (as illustrated in Figs. 1 and 2). Elevating the Ni to 15 at% leads to the development of an FCC phase rich in Ni and devoid of precipitation. Within this alloy, the BCC phase, characterized by a notable Cr content, accommodates cubic B2 precipitates of varying sizes. It's worth noting that TEM analysis identifies these B2 precipitates as enriched in Al and Ni (refer to Figs. 3 and 4). Further raising the Ni to 20 at% induces a pronounced increase in the proportion of the FCC phase, accompanied by the dispersed B2 precipitates. In a broader sense, the addition of Ni to the base composition brings the stabilization of the FCC phase and the formation of B2 precipitates, thus influencing the microstructural evolution of the alloy.

3.2. *Mechanical properties*

Provided the microstructural analysis in the prior sections, the mechanical properties can be understood through two key factors:

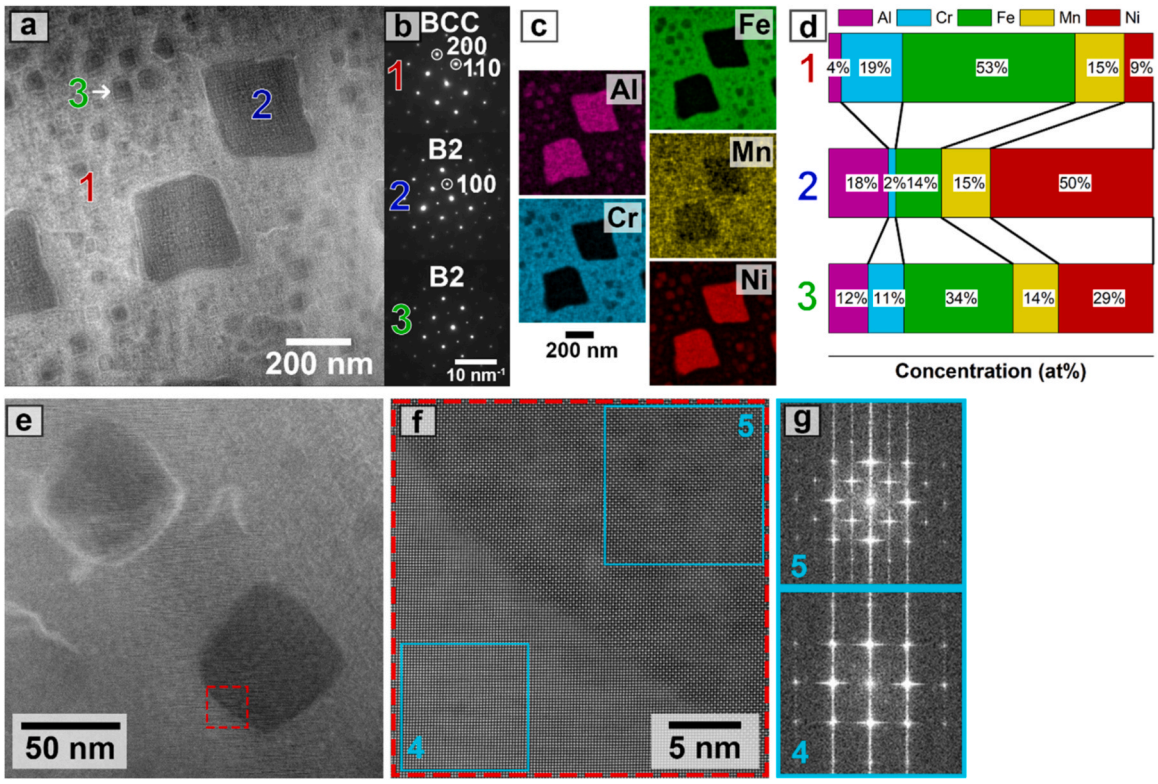

Fig. 4. (a) STEM micrograph of the 15 at% Ni MEA, (b) corresponding SAED patterns, (c) TEM-EDS measurements, (d) local chemical composition taken from TEM-EDS, (e) HR-STEM image of fine scale precipitate, (f) HR-STEM image of boundary between matrix and fine precipitate, and (g) FFT of HR-STEM image regions indicated in (f).

introduction of ordered phase precipitates and the formation of the FCC phase. Vickers hardness measurements shown in Fig. 5a indicate that with the addition of Ni, the hardness increases significantly from ~200 HV at 0 at% Ni, to ~475 HV at 10 at% Ni. This was most likely due to the precipitation of the ordered B2 phase in the microstructure, shown in other works to increase the hardness of other alloys via a precipitation hardening effect [9]. On addition of 15 at% Ni, XRD and EBSD demonstrated the presence of the FCC phase, emerging at grain boundaries and within grain interiors. This FCC phase formation reduced the hardness from ~475 HV at 10 at% Ni, to ~260 HV at 15 at % Ni. The presence of the BCC phase with B2 phase precipitates could explain why, even though the FCC phase composes 46% of the phase fraction (Fig. 3a), hardness remains higher than the single-phase BCC structure in the base $Al_{10}Cr_{15}(Fe_3Mn)_{75}$ MEA (~200 HV). As Ni content is increased to 20 at%, the hardness reduces to ~175 HV, likely the result of the high phase fraction of the ductile FCC phase (91% FCC, Fig. 3d).

The MEAs with lower Ni content of 0, 5, and 10 at% were unsuitable for tensile specimen fabrication due to cracking during machining caused by the brittle nature of the BCC phase. Fig. 5b shows the tensile stress-strain curves of the machinable 15 and 20 at% Ni MEAs at the homogenized state. The tensile measurements of the MEA with 15 at% Ni demonstrated a yield strength (YS) of 600 MPa, ultimate tensile strength (UTS) of 850 MPa, total elongation of 23%, and notably high specific strength of 84.4 MPa.cm^3/g. Even though the 15 at% Ni MEA remains in a homogenized state with a coarse grain size, it remarkably maintains a substantial primary strength of 600 MPa, outperforming numerous MEAs/HEAs and dual-phase steels in their as-cast or as-homogenized conditions. Nevertheless, it's noteworthy that the aged and processed MEAs/HEAs demonstrate significant promise for the

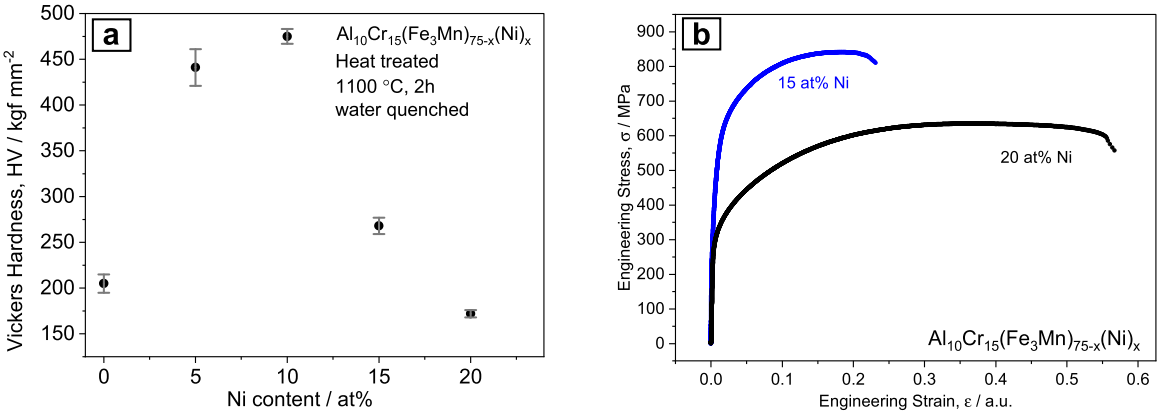

Fig. 5. (a) Vickers hardness measurements for the $Al_{10}Cr_{15}(Fe_3Mn)_{75-x}(Ni)_x$ MEAs as a function of Ni content, and (b) uniaxial stress-strain curves of the MEAs.

enhancement of mechanical performance, achieving exceptional properties particularly suited for high-temperature applications [21–23]. This elevated yield strength obtained in 15 at% Ni MEA could be attributed to a combination of factors, including the precipitation hardening effect of the B2 precipitates and the solid solution strengthening resulting from the incorporation of Ni within the FCC phase. In the plastic deformation domain, the presence of B2 precipitates along with lattice distortion within the phases contributes to the limitation of dislocation mobility. This restriction effectively bolsters both the overall strength and the capacity for strain hardening. In addition, this hierarchically heterogeneous microstructure, composed of soft FCC domain, hard BCC matrix, and ultrafine/nano-scaled ordered precipitates could impact on the strength/ductility of this MEA. The heterogeneity between domains can create strain partitioning into the structure under tensile stress, resulting in hetero-deformation induced (HDI) strengthening and HDI work hardening [24–27]. The heterogeneous structuring effect on the deformation behavior of the present MEA after a finely tuned thermo-mechanical processing will be addressed in detail in the future.

With an increase in the Ni content to 20 at%, the YS drops to 300 MPa; however, the total elongation notably increases to 56%. These changes in the mechanical performance could be attributed to the increase in the FCC phase fraction, resulting in significant improvements in ductility in exchange for strength. This MEA has significant work hardening capability by showing a uniform elongation of 45% with UTS of 600 MPa, which could be due to the interaction of the dislocations with the B2 precipitates [19,28].

3.3. Corrosion properties

To evaluate the effect of Ni addition on the corrosion performance in 0.6 M NaCl, electrochemical polarization measurements were performed, and the results are shown in Fig. 6a. These measurements demonstrate that increasing Ni content improves corrosion resistance through two key effects. First, corrosion potential shifts in the positive direction (E_{corr} = −0.756, −0.670, −0.585, −0.560 V vs. Ag/AgCl for 0, 5, 15, and 20 at% Ni, respectively), suggesting a more noble corrosion tendency. Second, pitting potential or resistance to steady-state pitting

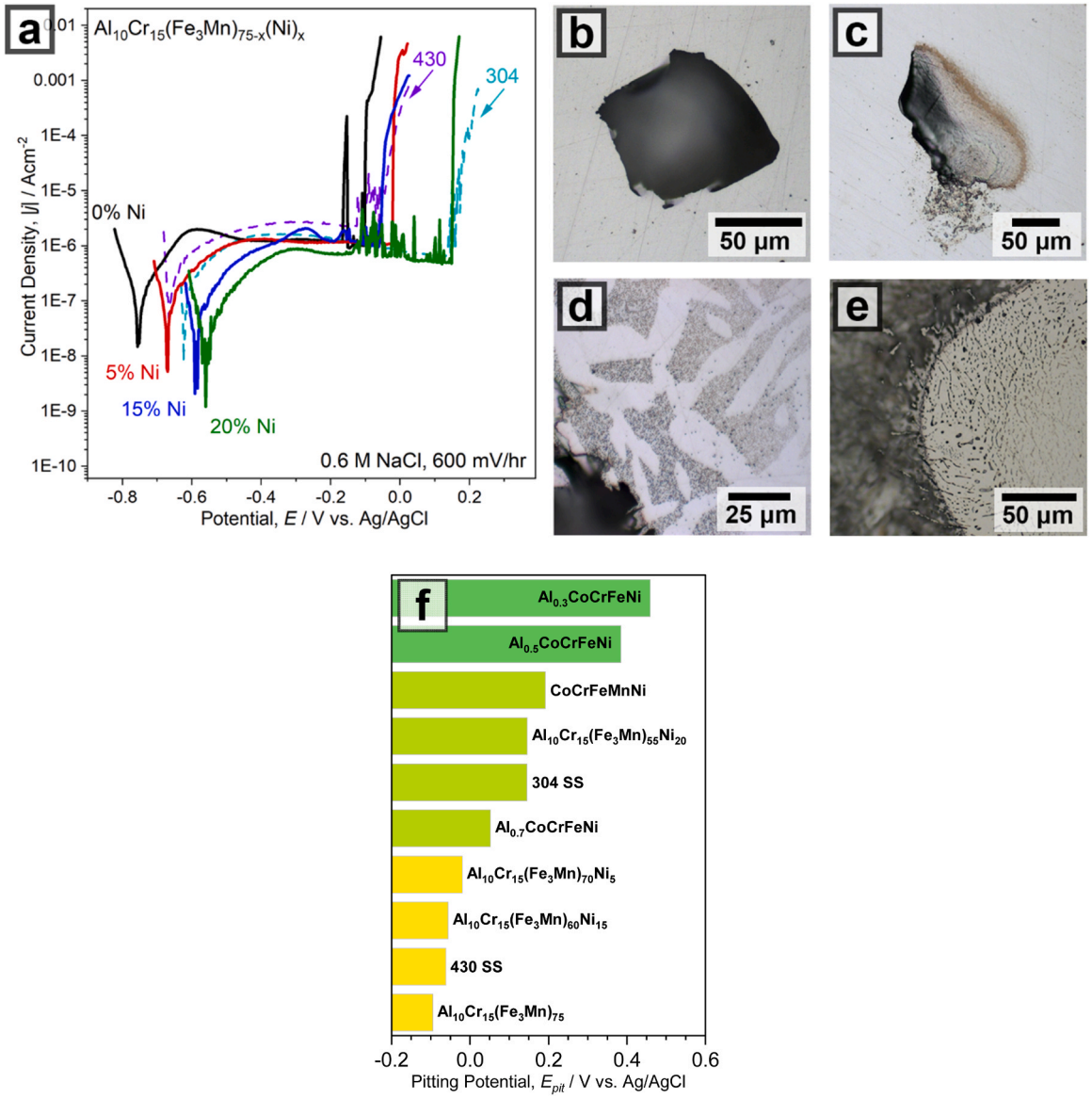

Fig. 6. (a) Electrochemical polarization measurements of the $Al_{10}Cr_{15}(Fe_3Mn)_{75-x}(Ni)_x$ MEAs, 304 and 430 stainless steels in 0.6 M NaCl solution; light optical micrographs of MEAs after polarization with (b) 0 at% Ni, (c) 5 at% Ni, (d) 15 at% Ni, (e) 20 at% Ni, and (f) comparison of pitting potential for the MEAs in this study to stainless steels and other HEAs [29,30].

corrosion, becomes more positive compared to the base alloy for all Ni contents (E_{pit} = −0.100, −0.05, −0.20, +0.146 vs. Ag/AgCl for 0, 5, 15, 20 at% Ni). In comparison to conventional stainless steels, the alloys with 0, 5, 15% Ni demonstrate corrosion resistance similar to 430 stainless steel (E_{pit} = −0.06 V vs. Ag/AgCl), while the 20 at% Ni MEA is comparable to 304 stainless steel (E_{pit} = 0.15 V vs. Ag/AgCl). However, the mechanism by which pitting resistance increases is not clear, especially in consideration of the post-corrosion morphology shown in Fig. 6b-e. For example, the alloys with 0 and 5 at% Ni (Fig. 6b and c) suggest that pitting corrosion does not appear to prefer any region of the microstructure. However, on increasing Ni to 15 at% (Fig. 6d), corrosion occurs preferentially in the BCC regions of the microstructure determined by EBSD (Fig. 3a), where Cr content is highest (Fig. 3c), but likely due to the presence of Al, Ni-rich and Cr-poor B2 precipitates (Fig. 4c) in this region. In studies of the effect of Al addition to both CrFeMnNi and CoCrFeNi alloys on corrosion resistance in chloride containing electrolytes, it has been observed that these Al-Ni rich sites are preferred for corrosion initiation due to their low Cr content [9,10].

Similarly, the alloy with 20 at% Ni (Fig. 6e) demonstrates failure due to preferential corrosion at the BCC phase (Fig. 3d), suggesting that the FCC phase has superior corrosion properties likely due to its high Cr content (Fig. 3 f) and the absence of precipitates. However, the polarization data for this composition shows numerous spikes in current density before steady-state pitting initiates, called metastable pitting, likely due to the corrosion of the Cr poor BCC phase. Based on these data, it is probable that the fully FCC phase alloy would have the greatest corrosion resistance at the cost of requiring additional Ni content.

Electrochemical polarization measurements were employed to determine the pitting potential of the MEAs and stainless steels, with the results presented in Fig. 6f. These outcomes were compared with measurements conducted by Shi et al. on $Al_xCoCrFeNi$ and Lu et al. on CoCrFeMnNi, all within a 0.6 M NaCl environment [29,30]. The data represents the 0, 5, and 15 at% Ni MEAs are comparable with 430 stainless steel, while the 20 at% Ni MEA aligns comparably with 304 stainless steel. Notably, these alloys' pitting resistance generally falls below that of CoCrFeMnNi and $Al_xCoCrFeNi$ alloys. This discrepancy could largely stem from the elevated Cr content in the CoCrFeMnNi and $Al_xCoCrFeNi$ alloys (≥20 at% Cr) when contrasted with the current MEAs. For instance, in $Al_xCoCrFeNi$ alloys, as Al content (x = 0.3, 0.5, 0.7) increases, there is a noticeable rise in both BCC and B2 phase fractions. This increment appears to correlate with a subsequent decrease in pitting resistance. Analogous to the $Al_xCrFeMnNi$ MEAs, this phenomenon was attributed to the differing Cr levels within the BCC and FCC phases. Consequently, augmenting the corrosion resistance of $Al_xCrFeMnNi$ MEAs could potentially be attained through the promotion of FCC phase formation.

4. Conclusions

In summary, this study explored the microstructure, mechanical properties, and corrosion properties of five homogenized MEAs to investigate the effect of systematic Ni addition on the $Al_{10}Cr_{15}(Fe_3Mn)_{75-x}(Ni)_x$ system. The results demonstrated the following: Ni addition results in the formation of B2 phase precipitates which lend high strength (YS = 600 MPa, UTS = 800 MPa at 15 at% Ni), while also stabilizing the FCC phase, which increases ductility in exchange for strength (elongation = 56%, YS = 300 MPa at 20 at% Ni). Ni addition also results in an improvement in corrosion resistance measured by increasing pitting resistance, but this appears to be driven primarily by the FCC phase fraction of the material, where increasing FCC content improves corrosion resistance significantly (E_{pit} = −0.05 V, F_{FCC} = 46% at 15 at% Ni; E_{pit} = 0.146 V, F_{FCC} = 91%), due to the poor Cr content of the BCC phase and associated B2 phase precipitates. These results demonstrate that a wide variety of microstructures are available with the potential for fine-tuning of mechanical and corrosion properties of the material through controlling Ni content. However, careful control of the B2 phase fraction and its chemistry are necessary to achieve the greatest corrosion performance due to the vulnerability of the B2 phase. Additionally, the intrinsic lightweight nature of these MEAs when contrasted with traditional steels, combined with their cost-effectiveness relative to HEAs/MEAs, with their appropriate basic mechanical properties, paves a promising path for the creation of innovative alloys with enhanced properties tailored for marine applications.

CRediT authorship contribution statement

Jarrod Gesualdi: Investigation, Visualization, Writing – original draft. **Peyman Asghari-Rad**: Investigation, Visualization, Conceptualization, Writing – original draft. **Erik Furton**: Investigation, Writing – review & editing. **Abhishek Singh**: Investigation. **Allison Beese**: Resources, Supervision, Writing – review & editing. **Hojong Kim**: Resources, Supervision, Project administration, Conceptualization, Funding acquisition, Writing – review & editing.

Declaration of Competing Interest

The authors declare that they have no known competing financial interests or personal relationships that could have appeared to influence the work reported in this paper.

Data Availability

Data will be made available on request.

Acknowledgements

The authors gratefully acknowledge the funding support of the Office of Naval Research (ONR), Award Number: N00014–19-1–2133 and US National Science Foundation (NSF), Award number: CMMI-1662817 and CMMI-1652575. The authors also would like to acknowledge Wes Auker and Dr. Ke Wang of the Penn State Material's Characterization Laboratory (MCL) for their assistance with the TEM work in this manuscript.

References

[1] J.W. Yeh, Recent progress in high-entropy alloys, Ann. Chim. Sci. Des. Mater. vol. 31 (6) (2006) 633–648, https://doi.org/10.3166/acsm.31.633-648.
[2] D.B. Miracle, O.N. Senkov, A critical review of high entropy alloys and related concepts, Acta Mater. vol. 122 (2017) 448–511, https://doi.org/10.1016/j.actamat.2016.08.081.
[3] B. Cantor, I.T.H. Chang, P. Knight, A.J.B. Vincent, Microstructural development in equiatomic multicomponent alloys, Mater. Sci. Eng. A vol. 375–377 (2004) 213–218, https://doi.org/10.1016/j.msea.2003.10.257.
[4] Z. Li, K.G. Pradeep, Y. Deng, D. Raabe, C.C. Tasan, Metastable high-entropy dual-phase alloys overcome the strength-ductility trade-off, Nature vol. 534 (7606) (2016) 227–230, https://doi.org/10.1038/nature17981.
[5] A. Munitz, L. Meshi, M.J. Kaufman, Heat treatments' effects on the microstructure and mechanical properties of an equiatomic Al-Cr-Fe-Mn-Ni high entropy alloy, Mater. Sci. Eng. A vol. 689 (February) (2017) 384–394, https://doi.org/10.1016/j.msea.2017.02.072.
[6] E. Ananiadis, K. Lentzaris, E. Georgatis, C. Mathiou, A. Poulia, A.E. Karantzalis, AlNiCrFeMn equiatomic high entropy alloy: a further insight in its microstructural evolution, mechanical and surface degradation response, Met. Mater. Int. vol. 26 (6) (2020) 793–811, https://doi.org/10.1007/s12540-019-00401-4.
[7] K. Masemola, P. Popoola, N. Malatji, The effect of annealing temperature on the microstructure, mechanical and electrochemical properties of arc-melted AlCrFeMnNi equi-atomic High entropy alloy, J. Mater. Res. Technol. vol. 9 (3) (2020) 5241–5251, https://doi.org/10.1016/j.jmrt.2020.03.050.
[8] Y. Chen, et al., Heavy ion irradiation effects on CrFeMnNi and AlCrFeMnNi high entropy alloys, J. Nucl. Mater. vol. 574 (2023), 154163, https://doi.org/10.1016/j.jnucmat.2022.154163.
[9] X. Chen, D. Gao, J.X. Hu, Y. Liu, C.P. Tang, Evolution of microstructures and properties in AlxCrFeMn0.8Ni2.1 HEAs, Met. Mater. Int. vol. 25 (5) (2019) 1135–1144, https://doi.org/10.1007/s12540-019-00282-7.
[10] Y. Shi, et al., Homogenization of AlxCoCrFeNi high-entropy alloys with improved corrosion resistance, Corros. Sci. vol. 133 (2018) 120–131, https://doi.org/10.1016/j.corsci.2018.01.030.
[11] S. Elkatatny, M.A.H. Gepreel, A. Hamada, K. Nakamura, K. Yamanaka, A. Chiba, Effect of Al content and cold rolling on the microstructure and mechanical

properties of Al5Cr12Fe35Mn28Ni20 high-entropy alloy, Mater. Sci. Eng. A vol. 759 (2019) 380–390, https://doi.org/10.1016/j.msea.2019.05.056.
[12] N.D. Stepanov, D.G. Shaysultanov, R.S. Chernichenko, M.A. Tikhonovsky, S. V. Zherebtsov, Effect of Al on structure and mechanical properties of Fe-Mn-Cr-Ni-Al non-equiatomic high entropy alloys with high Fe content, J. Alloy. Compd. vol. 770 (2019) 194–203, https://doi.org/10.1016/j.jallcom.2018.08.093.
[13] S.-T. Chen, et al., Microstructure and properties of age-hardenable AlxCrFe1.5MnNi0.5 alloys, Mater. Sci. Eng. A vol. 527 (2010) 5818–5825, https://doi.org/10.1016/j.msea.2010.05.052.
[14] L.J. Zhang, et al., The microstructure and mechanical properties of novel Al-Cr-Fe-Mn-Ni high-entropy alloys with trimodal distributions of coherent B2 precipitates, Mater. Sci. Eng. A vol. 757 (January) (2019) 160–171, https://doi.org/10.1016/j.msea.2019.04.104.
[15] G. Frankel, Pitting corrosion of metals, J. Electrochem. Soc. vol. 145 (6) (1998) 2186–2198, https://doi.org/10.1149/2.F03101if.
[16] ASTM International Standard, "Standard Test Method for Microindentation Hardness of Materials," no. E-384, pp. 1–24, 2017, doi:10.1520/E0384–17.
[17] ASTM, "Standard Reference Test Method for Making Potentiodynamic Anodic Polarization," no. G5–14, pp. 1–8, 2015, doi: 10.1520/G0005–14E01.2.
[18] M.H. Tsai, K.Y. Tsai, C.W. Tsai, C. Lee, C.C. Juan, J.W. Yeh, Criterion for sigma phase formation in Cr- and V-containing high-entropy alloys, Mater. Res. Lett. vol. 1 (4) (2013) 207–212, https://doi.org/10.1080/21663831.2013.831382.
[19] P. Sathiyamoorthi, et al., Achieving high strength and high ductility in $Al_{0.3}$CoCrNi medium-entropy alloy through multi-phase hierarchical microstructure, Materialia vol. 8 (2019), https://doi.org/10.1016/j.mtla.2019.100442.
[20] N.T.C. Nguyen, P. Asghari-Rad, P. Sathiyamoorthi, A. Zargaran, C.S. Lee, H.S. Kim, Ultrahigh high-strain-rate superplasticity in a nanostructured high-entropy alloy, Nat. Commun. vol. 11 (2020), https://doi.org/10.1038/s41467-020-16601-1.
[21] V. Shivam, et al., A novel Fe-rich non-equiatomic medium-entropy alloy with superior mechanical properties, J. Alloy. Compd. vol. 952 (2023), https://doi.org/10.1016/j.jallcom.2023.170029.
[22] V. Shivam, J. Basu, R. Manna, N.K. Mukhopadhyay, Local composition migration induced microstructural evolution and mechanical properties of non-equiatomic Fe40Cr25Ni15 Al15Co5 medium-entropy alloy, Metall. Mater. Trans. A vol. 52A (2021) 1777–1789, https://doi.org/10.1007/s11661-021-06188-7.
[23] S. Kar, V.C. Srivastava, G.K. Mandal, Low-density nano-precipitation hardened Ni-based medium entropy alloy with excellent strength-ductility synergy, J. Alloy. Compd. vol. 963 (2023), https://doi.org/10.1016/j.jallcom.2023.171213.
[24] P. Sathiyamoorthi, H.S. Kim, High-entropy alloys with heterogeneous microstructure: processing and mechanical properties, Prog. Mater. Sci. vol. 123 (2022), https://doi.org/10.1016/j.pmatsci.2020.100709.
[25] X. Wu, Y. Zhu, Heterogeneous materials: a new class of materials with unprecedented mechanical properties, Mater. Res. Lett. vol. 5 (8) (2017) 527–532, https://doi.org/10.1080/21663831.2017.1343208.
[26] M. Yang, Y. Pan, F. Yuan, Y. Zhu, X. Wu, Back stress strengthening and strain hardening in gradient structure, Mater. Res. Lett. vol. 4 (3) (2016) 145–151, https://doi.org/10.1080/21663831.2016.1153004.
[27] X. Wu, et al., Heterogeneous lamella structure unites ultrafine-grain strength with coarse-grain ductility, Proc. Natl. Acad. Sci. U. S. A. vol. 112 (47) (2015) 14501–14505, https://doi.org/10.1073/pnas.1517193112.
[28] P. Sathiyamoorthi, et al., Exceptional cryogenic strength-ductility synergy in $Al_{0.3}$CoCrNi medium-entropy alloy through heterogeneous grain structure and nano-scale precipitates (no.), Mater. Sci. Eng. A vol. 766 (2019), https://doi.org/10.1016/j.msea.2019.138372 (no.).
[29] Y. Shi, B. Yang, X. Xie, J. Brechtl, K.A. Dahmen, P.K. Liaw, Corrosion of Al_xCoCrFeNi high-entropy alloys: Al-content and potential scan-rate dependent pitting behavior, Corros. Sci. vol. 119 (2017) 33–45, https://doi.org/10.1016/j.corsci.2017.02.019.
[30] C.W. Lu, Y.S. Lu, Z.H. Lai, H.W. Yen, Y.L. Lee, Comparative corrosion behavior of Fe50Mn30Co10Cr10 dual-phase high-entropy alloy and CoCrFeMnNi high-entropy alloy in 3.5 wt% NaCl solution, J. Alloy. Compd. vol. 842 (2020), https://doi.org/10.1016/j.jallcom.2020.155824.